The Science of Compliance: Continuous Fiber Angle Topology Optimization with Stress Constraints and Path-Planning

C. Troelsgaard, F. Østergaard, F. Elmstrøm, J. L. Hansen, R. K. Schøn

Department of Materials and Production, Aalborg University
Fibigerstraede 16, DK-9220 Aalborg East, Denmark
Email: {ctroel19, faster19, felmst19, jh19, rschan19}@student.aau.dk,
Web page: http://www.mechman.mp.aau.dk/

Abstract
Continuous Fiber Co-extrusion (CFC) is a versatile manufacturing technology, that provides large design freedom for composite structures. Through simultaneous Continuous Fiber Angle and Topology Optimization (CFATO), this may be utilized. Although CFATO has received much attention, a solution is not commercially available. This paper seeks a workflow from a design domain to a printed component with an optimized fiber layout. The CFATO minimizes compliance, subject to mass and Tsai-Wu failure index constraints. An angle filter is incorporated in the optimization. Four streamline path-planning schemes are investigated and used to generate manufacturing-tolerant paths, which are subsequently 3D-printed using a custom G-code generation tool. The results show that the optimization scheme minimizes compliance while adhering to the constraints, by alleviating geometrically induced stress concentrations. The angle filter was able to produce primarily smooth fiber orientations, except in interfaces between compressive- and tensile-stressed members. Streamline paths have inherent discontinuities regardless of the scheme used, however, an optimized design was realized by CFC 3D printing.

Keywords: Topology Optimization, Fiber Angle Optimization, Additive Manufacturing, Continuous Fiber Reinforced 3D Printed Composites, Stress-Constrained Optimization, Angle Filtering, Path-Planning

1. Introduction

Continuous Fiber Co-extrusion (CFC) is a versatile additive manufacturing technique that gives extensive design freedom of composite structures. In the present work, a framework for developing and manufacturing compliance-optimized designs of such structures, subject to stress and mass constraints, will be investigated. An Anisoprint Composer A4 3D printer is used for manufacturing.

Topology Optimization (TO) is a design tool typically used for high-performance structures in e.g. aerospace applications [1]. The inclusion of high-performance materials, such as carbon fiber-reinforced polymers, is therefore of interest. In the context of this work, the focus is solely on the continuous fiber-reinforced materials, offered by CFC. TO of continuous fiber-reinforced structures has received much attention, [2] [3] [4], however, to the authors' knowledge there is no commercially available method for performing such optimization and a slicing software capable of ensuring its manufacturability, thus limiting its industrial applications.

The objective is therefore twofold: Develop a general-purpose TO of a continuous fiber-reinforced material and a method capable of 3D printing the optimized structure using CFC.

TO became a popular method after [5] showed that a simple finite element program and OC criterion are sufficient for developing a functional algorithm. Due to numerical efficiency, linear elements are often used. This caused checkerboarding, due to the artificial stiffness introduced by linear elements [4]. It can be solved using higher order elements as suggested by [6]. Due to computational efficiency, filtering techniques are the most popular solution to eliminate checkerboarding. The sensitivity filter by [7] solves checkerboarding, but can cause inconsistent sensitivities. The linear filter proposed by [8] and [9] is often used since it solves the checkerboarding problem and yields consistent sensitivities. Furthermore, mesh-independent solutions are obtained. Discrete Material Optimization (DMO) by [10] has been widely used due to its applicability for laminated structures. [3] introduced the fiber angles through the constitutive matrix using the transformation matrices from the material coordinate system to the global Cartesian coordinate system in simultaneous

Continuous Fiber Angle and Topology Optimization (CFATO). For low-shear stiffness orthotropic materials, the minimum compliance is achieved when the principal material direction and largest principal strain direction are aligned [11]. However, this may not necessarily be feasible, if introducing multiple load cases, orientation smoothing or stress constraints.

Adaptive constraint scaling was introduced by [12] in order to estimate the actual stress value when an aggregated function is used in stress-based topology optimization. The adaptive constraint scaling algorithm is further explained by [13]. [14] introduced the Tsai-Wu failure criteria into DMO using the failure index and reduced the number of constraints with an aggregated function. Often the aggregation approaches used are Kreisselmeier-Steinhauser and P-norm, since these do not require a weight function study. However, the local control of the element-wise stress state is lost and the problem becomes more non-linear [13]. [15] successfully implemented the Tsai-Wu criterion which scales quadratically with the load. The failure index formulation scales linearly with the applied load which is preferable from an engineering perspective. Relaxation techniques such as the ε-approach by [16] and qp-approach by [17] are widely used in stress-based optimization to avoid singular optimum. The stress of elements with intermediate densities is penalized, such that for binary material densities, it converges to the stress state of the original problem. According to [18] the qp-approach is preferable in gradient-based optimization since the approximation of the original problem is more smooth. In order to ensure structural integrity, manufacturing uncertainties can be considered using a threshold projection filter to generate dilated, intermediate and eroded densities as proposed by [19].

To ensure manufacturability, the resulting design must have a smoothly varying fiber orientation. [2] proposed a linear unit vector filtering approach, where the periodicity of the element stiffness is taken into account.

Some methods have been proposed to generate print paths for manufacturing the optimized design. Widely used is the contour method, which bases print paths on external contours rather than the optimized fiber orientations. This approach has been used in [3] and [20]. Alternatively, streamline algorithms use the optimized fiber angles as input for path-planning. Streamlines are commonly used to visualize flow fields by supplying a 'seed point' and tracing a particle through the flow field. [21] and [22] use streamline placement algorithms to successfully obtain printable paths from TO results. Both approaches smooth the fiber angles prior to path-planning, changing the angles obtained by CFATO. Furthermore, paths obtained have fiber discontinuities that create stress concentrations not taken into account during CFATO. [21] proposes seeding based on maximum element stresses, whereas [22] initializes a seed list from the nodes of each element, subsequently creating new seeds based on established streamlines. [22] proposes other strategies such as farthest point seeding to generate longer streamlines.

2. Methodology: Pre-processing and CFATO

The framework for this paper is illustrated in Fig. 1.

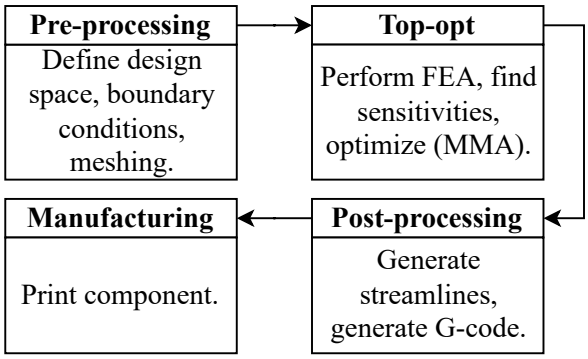

Fig. 1 Paper framework.

2.1 Pre-processing

The design domain is defined and discretized in ANSYS workbench and then exported. The model is imported to MATLAB using a modified version of ANSYSimport by [23]. Passive elements are used to avoid removing material from certain areas. This is done by removing only the density from the design variables. In order to have an arbitrary design domain an isoparametric element formulation is used, thereby supporting general unstructured meshes.

2.2 Topology and Fiber Angle Optimization

In order to model the orthotropic behavior, the isoparametric element stiffness matrix $[\mathbf{k_0}]$ is calculated as shown in Eq. (1) according to [24].

$$[\mathbf{k_0}] = \int_{-1}^{1}\int_{-1}^{1} [\mathbf{B}]^T \left[\bar{\mathbf{Q}}\right] [\mathbf{B}]\, Jtd\eta d\xi \qquad (1)$$

Which is evaluated with a second-order Gauss quadrature (full integration). $[\mathbf{B}]$ is the 2D strain-displacement

matrix, J is the determinant of the Jacobian and t is the thickness of the element.

$\left[\bar{\mathbf{Q}}\right]$ expresses the constitutive properties of an orthotropic material in the global coordinate system. The rotation between the material and the global coordinate system is determined using Eq. (2)

$$\left[\bar{\mathbf{Q}}\right] = \left[\mathbf{T}\right]^{-1}\left[\mathbf{Q}\right]\left[\mathbf{T}\right]^{-T} \tag{2}$$

$[\mathbf{Q}]$ is the orthotropic constitutive matrix in the material coordinate system as shown in Eq. (3) and $[\mathbf{T}]$ is the rotation matrix which is given in Eq. (4)

$$[\mathbf{Q}] = \begin{bmatrix} \frac{E_1}{1-\nu_{12}\nu_{21}} & \frac{\nu_{21}E_1}{1-\nu_{12}\nu_{21}} & 0 \\ \frac{\nu 21 E_1}{1-\nu_{12}\nu_{21}} & \frac{E_2}{1-\nu_{12}\nu_{21}} & 0 \\ 0 & 0 & G_{12} \end{bmatrix} \tag{3}$$

In Eq. (3) E_1, E_2, G_{12}, ν_{12} and ν_{21} is Young's modulus in the longitudinal and transverse fiber-direction, the shear modulus, major and minor Poisson's ratio respectively.

$$[\mathbf{T}] = \begin{bmatrix} c^2 & s^2 & 2cs \\ s^2 & c^2 & -2cs \\ -cs & cs & c^2 - s^2 \end{bmatrix} \tag{4}$$

In Eq. (4), c and s denotes $\cos\theta$ and $\sin\theta$ respectively. θ is the positive angle between the global and material coordinate system [25].

2.2.1 Optimization Formulation

The entry number in vectors is indicated by a subscript, whereas for matrices, it is denoted by a superscript of column and row. n_{elm} is the number of elements. The optimization problem is given in Eq. (5).

$$\underset{\{\boldsymbol{\rho}\},\{\boldsymbol{\theta}\}}{\text{Minimize}} \quad c(\{\tilde{\boldsymbol{\rho}}\},\{\tilde{\boldsymbol{\theta}}\}) = \sum_{i=1}^{n_{elm}} \{\mathbf{d}\}_i^T \left[\mathbf{k}\right]_i \{\mathbf{d}\}_i \tag{5a}$$

$$\text{Subject to} \quad [\mathbf{K}]\{\mathbf{D}\} = \{\mathbf{F}\} \tag{5b}$$

$$g_1(\{\tilde{\tilde{\boldsymbol{\rho}}}\}) = \frac{\sum_{i=1}^{n_{elm}} \tilde{\tilde{\rho}}_i V_i}{V_0 \sum_{i=1}^{n_{elm}} V_i} - 1 \leq 0 \tag{5c}$$

$$g_2(\{\tilde{\tilde{\boldsymbol{\rho}}}\},\{\tilde{\boldsymbol{\theta}}\}) = \psi^{(k)} g_{pn} - 1 \leq 0 \tag{5d}$$

$$\{\mathbf{0}\} \leq \{\boldsymbol{\rho}\} \leq \{\mathbf{1}\} \tag{5e}$$

$$-\{\boldsymbol{\pi}\} \leq \{\boldsymbol{\theta}\} \leq \{\boldsymbol{\pi}\} \tag{5f}$$

($\{\tilde{\tilde{\boldsymbol{\rho}}}\}$,$\{\tilde{\boldsymbol{\theta}}\}$) and ($\{\boldsymbol{\rho}\}$,$\{\boldsymbol{\theta}\}$) are the filtered and unfiltered design variables, respectively. The objective, Eq. (5a), is a function of the filtered design variables, subject to equilibrium, Eq. (5b). Eq. (5c) is the volume constraint, where V_i is the element volume and V_0 is the desired volume fraction. Eq. (5d) is the stress constraint, where g_{pn} is the aggregation function and ψ_i is a scaling factor. Eq. (5e) and Eq. (5f) are the design variable bounds. To avoid singularity of the stiffness matrix, the modified SIMP approach is used Eq. (6) [19]. $\rho_{min} = 10^{-3}$ and $p = 3$.

$$\left[\mathbf{k}\right]_i = (\rho_{min} + (1-\rho_{min})\tilde{\tilde{\rho}}_i^p)\left[\mathbf{k_0}\right]_i \tag{6}$$

The optimization will be done by the Method of Moving Asymptotes (MMA) [26].

2.2.2 Filtering

In order to circumvent mesh-dependency, checkerboarding and enforce a minimum length scale for manufacturing considerations, a linear density filter analogous to [9] is employed, in Eq. (7).

$$\tilde{\rho}_i = \frac{\sum_{j\in N_i} H^{(i,j)}\rho_j}{\sum_{j\in N_i} H^{(i,j)}} \tag{7a}$$

Where:

$$H^{(i,j)} = V_j \max\left(0, r - \sqrt{(x_i - x_j)^2 + (y_i - y_j)^2}\right) \tag{7b}$$

(x,y) are the center coordinates of the elements and N_i is the set containing the indices of elements within the filter radius r of the i^{th} element.

To reduce intermediate densities, the threshold projection filter shown in Eq. (8) with a continuation approach described in [19] is applied. β is doubled every 10^{th} iteration until it reaches the maximum value, $\beta_{max} = l_e/r$, as suggested by [19] to avoid stress concentrations due to an excessively discrete model. l_e is the characteristic element length. Densities lower than the threshold value κ are driven toward 0 and values above toward 1. The projection parameter β determine the steepness of the projection. At $\beta = 0$ the filter act as a linear projection. When $\beta \to \infty$ the filter becomes a Heaviside step function.

$$\tilde{\tilde{\rho}}_i = \frac{\tanh(\beta\kappa) + \tanh(\beta(\tilde{\rho}_i - \kappa))}{\tanh(\beta\kappa) + \tanh(\beta(1-\kappa))} \tag{8}$$

To smooth the fiber orientations, a linear angle filtering inspired by [2] is implemented, as given in Eq. (9a).

$$\tilde{\theta}_i = \arctan\frac{\sum_{j\in N_i} \alpha^{(i,j)} H^{(i,j)} \rho_j^p \sin\theta_j}{\sum_{j\in N_i} \alpha^{(i,j)} H^{(i,j)} \rho_j^p \cos\theta_j} \tag{9a}$$

Where:

$$\alpha^{(i,j)} = \begin{cases} 1, & \text{if } \cos(\theta_i - \theta_j) \geq 0 \\ -1, & \text{if } \cos(\theta_i - \theta_j) < 0 \end{cases} \tag{9b}$$

$\alpha^{(i,j)}$ is calculated to account for the periodicity of the constitutive properties in each element. As opposed to [2], the penalized density design variable is included in Eq. (9a), to reduce the contribution of inactive elements.

2.2.3 Tsai-Wu Constraint

In order to obtain the failure index the Tsai-Wu scaling factor γ is introduced to convert the criterion to a second-order polynomial equation as shown in Eq. (10).

$$\begin{aligned} 0 =&\gamma^2(F_{11}\sigma_1^2 + F_{22}\sigma_2^2 + 2F_{12}\sigma_1\sigma_2 + F_{66}\sigma_6^2)+ \\ &\gamma(F_1\sigma_1 + F_2\sigma_2) - 1 = \gamma^2 a + \gamma b - 1 \end{aligned} \tag{10}$$

γ is calculated for each element $\gamma = \frac{-b+\sqrt{d}}{2a}$, where $d = b^2 + 4a$. The strength values are determined using the compression and tension strength in the fiber direction X_c, X_t and transverse direction Y_c, Y_t as defined in [25]:

$$F_1 = \frac{1}{X_t} - \frac{1}{X_c}, \qquad F_2 = \frac{1}{Y_t} - \frac{1}{Y_c}, \qquad F_{11} = \frac{1}{X_t X_c}$$
$$F_{11} = \frac{1}{Y_t Y_c}, \qquad F_{12} \approx -\frac{1}{2}\sqrt{F_{11}F_{22}}, \qquad F_{66} = \frac{1}{S^2}$$

The failure index is determined by equation Eq. (11). γ is the smallest positive root of Eq. (10).

$$FI = \frac{1}{\gamma} \tag{11}$$

The failure index is relaxed using the qp-approach as shown in Eq. (12)

$$FI_{rel} = w(\tilde{\tilde{\rho}})FI = \tilde{\tilde{\rho}}^{p-q}FI \tag{12}$$

The stress penalization factor is set to $q = 2.5$, to fulfill the relation $p > q$ proposed by [17]. The relaxed failure indices are formulated as a P-norm aggregate function as shown in Eq. (13) to transform the local criterion into a global criterion.

$$g_{pn} = \left(\sum_{e=1}^{n_{elm}} \left(FI_{rel_e}\right)^P \right)^{\frac{1}{P}} \tag{13}$$

The P-norm converges to the maximum Tsai-Wu failure index, as P approaches infinity. Large values of P can cause numerical problems. To improve the accuracy and allow higher P-values, the adaptive constraint scaling implementation by [13] is used.

$$g_{max} = \psi^{(k)} g_{pn} \tag{14}$$

The adaptive scaling factor $\psi^{(k)}$ is calculated in each iteration as shown in Eq. (15). $\psi^{(k)}$ converges to a constant value through the optimization and is therefore assumed independent of the design variables.

$$\psi^{(k)} = \vartheta^{(k)} \left(\frac{\max(FI_{rel}^{(k-1)})}{g_{pn}^{(k-1)}} \right) + (1 - \vartheta^{(k)})\psi^{(k-1)} \tag{15}$$

$\max(FI_{rel}^{(k-1)})$ is the maximum relaxed failure index of an element. $g_{pn}^{(k-1)}$ is the previous value of the P-norm aggregate function. ϑ is an adaptive numerical damping coefficient that depends on the numerical oscillation. For more information see [13].

2.2.4 Sensitivities

The compliance sensitivity of the unfiltered densities can be calculated by applying the chain rule of differentiation, as in Eq. (16).

$$\frac{\partial c}{\partial \rho_e} = \sum_{i \in N_e} \frac{\partial c}{\partial \tilde{\tilde{\rho}}_i} \frac{\partial \tilde{\tilde{\rho}}_i}{\partial \tilde{\rho}_i} \frac{\partial \tilde{\rho}_i}{\partial \rho_e} \tag{16}$$

The first term can be shown to be Eq. (17), by use of the adjoint method.

$$\frac{\partial c}{\partial \tilde{\tilde{\rho}}_i} = -p(1 - \rho_{min})\tilde{\tilde{\rho}}_i^{p-1} \{\mathbf{d}\}_i^T [\mathbf{k}]_i \{\mathbf{d}\}_i \tag{17}$$

The second term is the partial derivative of Eq. (8) and is given in Eq. (18).

$$\frac{\partial \tilde{\tilde{\rho}}_i}{\partial \tilde{\rho}_i} = \frac{\beta \operatorname{sech}(\beta\tilde{\rho}_i - \kappa)^2}{\tanh \beta\kappa + \tanh(\beta - \beta\kappa)} \tag{18}$$

The third term is the partial derivative of Eq. (7), and is given as in Eq. (19).

$$\frac{\partial \tilde{\rho}_i}{\partial \rho_e} = \frac{H^{(i,e)}}{\sum_{j \in N_i} H^{(i,j)}} \tag{19}$$

The compliance sensitivity of the unfiltered angles can be calculated as in Eq. (20).

$$\frac{\partial c}{\partial \theta_e} = \sum_{i \in N_e} \frac{\partial c}{\partial \tilde{\theta}_i} \frac{\partial \tilde{\theta}_i}{\partial \theta_e} \tag{20}$$

Analogous to the densities, the first term can be shown to be Eq. (21), by use of the adjoint method.

$$\frac{\partial c}{\partial \tilde{\theta}_i} = -\left(\rho_{min} + (1 - \rho_{min})\tilde{\tilde{\rho}}_i^p\right) \{\mathbf{d}\}_i^T \frac{\partial [\mathbf{k}]_i}{\partial \tilde{\theta}_i} \{\mathbf{d}\}_i \tag{21}$$

Where:

$$\frac{\partial [\mathbf{k}]_i}{\partial \tilde{\theta}_i} = \int_{-1}^{1}\int_{-1}^{1} [\mathbf{B}]^T \left(\frac{\partial [\mathbf{T}]^{-1}}{\partial \tilde{\theta}_i} [\mathbf{Q}] [\mathbf{T}]^{-T} + [\mathbf{T}]^{-1} [\mathbf{Q}] \frac{\partial [\mathbf{T}]^{-T}}{\partial \tilde{\theta}_i} \right) [\mathbf{B}] \, Jtd\eta d\xi$$

The second term is the derivative of Eq. (9a). $\partial \alpha^{(i,j)} / \partial \theta_i$ is only nonzero when θ_i and θ_j are exactly orthogonal, in which case the derivative is infinite, thus $\alpha^{(i,j)}$ is treated as a constant. The derivative can be

computed as shown in Eq. (22), by applying the chain rule of differentiation.

$$\frac{\partial\tilde{\theta}_i}{\partial\theta_e} = \frac{\frac{\alpha^{(i,e)}H^{(i,e)}\rho_e^p\cos\theta_e}{\sum_{j\in N_i}\alpha^{(i,j)}H^{(i,j)}\rho_j^p\cos\theta_j}}{\left(\frac{\sum_{j\in N_i}\alpha^{(i,j)}H^{(i,j)}\rho_j^p\sin\theta_j}{\sum_{j\in N_i}\alpha^{(i,j)}H^{(i,j)}\rho_j^p\cos\theta_j}\right)^2+1} + \frac{\frac{\alpha^{(i,e)}H^{(i,e)}\rho_e^p\sin\theta_e\sum_{j\in N_i}\alpha^{(i,j)}H^{(i,j)}\rho_j^p\sin\theta_j}{(\sum_{j\in N_i}\alpha^{(i,j)}H^{(i,j)}\rho_j^p\cos\theta_j)^2}}{\left(\frac{\sum_{j\in N_i}\alpha^{(i,j)}H^{(i,j)}\rho_j^p\sin\theta_j}{\sum_{j\in N_i}\alpha^{(i,j)}H^{(i,j)}\rho_j^p\cos\theta_j}\right)^2+1} \tag{22}$$

The derivative of the volume constraint can be calculated as in Eq. (23).

$$\frac{\partial g_1}{\partial\rho_e} = \sum_{i\in N_e}\frac{\partial g_1}{\partial\tilde{\tilde{\rho}}_i}\frac{\partial\tilde{\tilde{\rho}}_i}{\partial\tilde{\rho}_i}\frac{\partial\tilde{\rho}_i}{\partial\rho_e} \tag{23}$$

The first term can be calculated as in Eq. (24).

$$\frac{\partial g_1}{\partial\tilde{\tilde{\rho}}_i} = \frac{V_i}{V_0\sum_{i=1}^{n_{elm}}V_i} \tag{24}$$

The second and third term of Eq. (23) is already computed in Eq. (18) and Eq. (19). The stress constraint is a function of the state variable $\{\mathbf{D}\}$ and the design variables $\{\mathbf{x}\}$, which include both ρ and θ, through $g_{max}\left(\{\mathbf{D}(\{\mathbf{x}\})\},\{\mathbf{x}\}\right)$. The sensitivities are determined using the adjoint method. The augmented function is formulated using the Lagrange multiplier method as shown in Eq. (25).

$$\begin{aligned}\bar{g}_{max} = g_{max}(\{\mathbf{D}(\{\mathbf{x}\})\},\{\mathbf{x}\}) - \\ \{\boldsymbol{\lambda}\}^T([\mathbf{K}]\{\mathbf{D}\}-\{\mathbf{F}\})\end{aligned} \tag{25}$$

If the force is assumed to be independent of the design variables, then the derivative of the augmented function can be determined as shown in Eq. (26).

$$\begin{aligned}\frac{d\bar{g}_{max}}{dx_i} = \left(\frac{\partial g_{max}}{\partial\{\mathbf{D}\}} - \{\boldsymbol{\lambda}\}^T[\mathbf{K}]\right)\frac{\partial\{\mathbf{D}\}}{\partial x_i} \\ + \frac{\partial g_{max}}{\partial x_i} - \{\boldsymbol{\lambda}\}^T\frac{\partial[\mathbf{K}]}{\partial x_i}\{\mathbf{D}\}\end{aligned} \tag{26}$$

The adjoint vector $\{\boldsymbol{\lambda}\}$ can be freely determined since the added term in the augmented function is stated on residual form: $[\mathbf{K}]\{\mathbf{D}\}-\{\mathbf{F}\}=\{\mathbf{0}\}$. Therefore an adjoint vector that satisfies Eq. (27) is chosen.

$$[\mathbf{K}]\{\boldsymbol{\lambda}\} = \left(\frac{\partial g_{max}}{\partial\{\mathbf{D}\}}\right)^T \tag{27}$$

When Eq. (27) is solved the derivative of the Tsai-Wu constraint reduces to Eq. (28)

$$\frac{d\bar{g}_{max}}{dx_i} = \frac{\partial g_{max}}{\partial x_i} - \{\boldsymbol{\lambda}\}^T\frac{\partial[\mathbf{K}]}{\partial x_i}\{\mathbf{D}\} \tag{28}$$

$\frac{\partial g_{max}}{\partial\{\mathbf{D}\}}$ can be determined applying the chain rule as shown in Eq. (29)

$$\begin{aligned}\frac{\partial g_{max}}{\partial\{\mathbf{D}\}} = \psi^{(k)}\sum_{e=1}^{n_{elm}}\frac{\partial g_{pn}}{\partial FI_{rel_e}}\frac{\partial FI_{rel_e}}{\partial FI_e} \\ \left(\frac{\partial FI_e}{\partial\{\boldsymbol{\sigma_{12}}\}_e}\right)^T\frac{\partial\{\boldsymbol{\sigma_{12}}\}_e}{\partial\{\boldsymbol{\sigma_{xy}}\}_e}\frac{\partial\{\boldsymbol{\sigma_{xy}}\}_e}{\partial\{\mathbf{D}\}}\end{aligned} \tag{29}$$

The individual terms in Eq. (29) can be determined as

$$\frac{\partial g_{pn}}{\partial FI_{rel_e}} = FI_{rel_e}^{P-1}\left(\sum_{e=1}^{n_{elm}}(FI_{rel_e})^P\right)^{\frac{1}{P}-1} \tag{30}$$

$$\frac{\partial FI_{rel_e}}{\partial FI_e} = \frac{\partial}{\partial FI}\left(w(\tilde{\tilde{\rho}})FI\right) = w(\tilde{\tilde{\rho}}) = \tilde{\tilde{\rho}}^{p-q} \tag{31}$$

$$\begin{aligned}\frac{\partial FI_e}{\partial\{\boldsymbol{\sigma_{12}}\}_e} = \frac{\partial FI}{\partial\gamma}\left(\frac{\partial\gamma}{\partial a}\frac{\partial a}{\partial\{\boldsymbol{\sigma_{12}}\}} + \frac{\partial\gamma}{\partial b}\frac{\partial b}{\partial\{\boldsymbol{\sigma_{12}}\}} + \right. \\ \left.\frac{\partial\gamma}{\partial d}\left(\frac{\partial d}{\partial a}\frac{\partial a}{\partial\{\boldsymbol{\sigma_{12}}\}} + \frac{\partial d}{\partial b}\frac{\partial b}{\partial\{\boldsymbol{\sigma_{12}}\}}\right)\right)\end{aligned} \tag{32}$$

$$\frac{\partial\{\boldsymbol{\sigma_{12}}\}_e}{\partial\{\boldsymbol{\sigma_{xy}}\}_e} = \frac{\partial}{\partial\{\boldsymbol{\sigma_{xy}}\}_e}\left([\mathbf{T}]\{\boldsymbol{\sigma_{xy}}\}_e\right) = [\mathbf{T}] \tag{33}$$

$$\frac{\partial\{\boldsymbol{\sigma_{xy}}\}_e}{\partial\{\mathbf{D}\}} = \frac{\partial}{\partial\{\mathbf{D}\}}\left(\left[\bar{\mathbf{Q}}\right][\mathbf{B}][\mathbf{L}]_e\{\mathbf{D}\}\right) = \left[\bar{\mathbf{Q}}\right][\mathbf{B}][\mathbf{L}]_e \tag{34}$$

$[\mathbf{L}]_e$ is a $8\times N_{DoF}$ sparse bookkeeping matrix with 0 in all entries except those that extract the nodal displacements: $\{\mathbf{d}\}_e = [\mathbf{L}]_e\{\mathbf{D}\}$ are 1. The partial derivatives of the constraint w.r.t the design variables need to be determined. Applying the chain rule as shown in Eq. (35)

$$\frac{\partial g_{max}}{\partial\rho_j} = \sum_{i\in N_j}\frac{\partial g_{max}}{\partial\tilde{\tilde{\rho}}_i}\frac{\partial\tilde{\tilde{\rho}}_i}{\partial\tilde{\rho}_i}\frac{\partial\tilde{\rho}_i}{\partial\rho_j} \tag{35}$$

$$\frac{\partial g_{max}}{\partial\tilde{\tilde{\rho}}_i} = \psi^{(k)}\frac{\partial g_{pn}}{\partial FI_{rel_i}}\frac{\partial FI_{rel_i}}{\partial w(\tilde{\tilde{\rho}}_i)}\frac{\partial w(\tilde{\tilde{\rho}}_i)}{\partial\tilde{\tilde{\rho}}_i} \tag{36}$$

$\frac{\partial g_{pn}}{\partial FI_{rel_e}}$ is calculated using Eq. (30). The last terms are calculated as shown in Eq. (37) and Eq. (38)

$$\frac{\partial FI_{rel_e}}{\partial w(\tilde{\tilde{\rho}}_e)} = FI_e \tag{37}$$

$$\frac{\partial w(\tilde{\tilde{\rho}}_e)}{\partial\tilde{\tilde{\rho}}_e} = (p-q)\tilde{\tilde{\rho}}_e^{p-q-1} \tag{38}$$

The partial derivative w.r.t. the fiber angles $\frac{\partial g_{max}}{\partial \theta_j}$ is determined using the chain rule as shown in Eq. (39).

$$\frac{\partial g_{max}}{\partial \theta_j} = \sum_{i \in N_j} \frac{\partial g_{max}}{\partial \tilde{\theta}_i} \frac{\partial \tilde{\theta}_i}{\partial \theta_j} \tag{39}$$

$$\frac{\partial g_{max}}{\partial \tilde{\theta}_i} = \psi^{(k)} \frac{\partial g_{pn}}{\partial FI_{rel_i}} \frac{\partial FI_{rel_i}}{\partial FI_i} \left(\frac{\partial FI_i}{\partial \{\boldsymbol{\sigma_{12}}\}_i} \right)^T \frac{\partial \{\boldsymbol{\sigma_{12}}\}_i}{\partial \tilde{\theta}_i} \tag{40}$$

The terms in Eq. (40), $\frac{\partial g_{pn}}{\partial FI_{rel_e}}$, $\frac{\partial FI_{rel_e}}{\partial FI_e}$ and $\frac{\partial FI_e}{\partial \{\boldsymbol{\sigma_{12}}\}_e}$ are calculated as shown in Eq. (30) (31) and (32). Applying the product rule then the derivative of the stress in the material coordinate system w.r.t. the fiber angles is determined using Eq. (41)

$$\frac{\partial \{\boldsymbol{\sigma_{12}}\}_i}{\partial \tilde{\theta}_i} = [\mathbf{Q}] \frac{\partial \left([\mathbf{T}]^{-T} \right)}{\partial \tilde{\theta}_i} [\mathbf{B}] \{\mathbf{d}\}_e \tag{41}$$

The analytical sensitivities have been validated using a finite difference approximation.

3. Numerical Test Case

The L-bracket, see Fig. 2, is a popular benchmark example used in stress-constrained TO, and will be adopted in this work. The material parameters used in the optimization scheme can be seen in Tab. I.

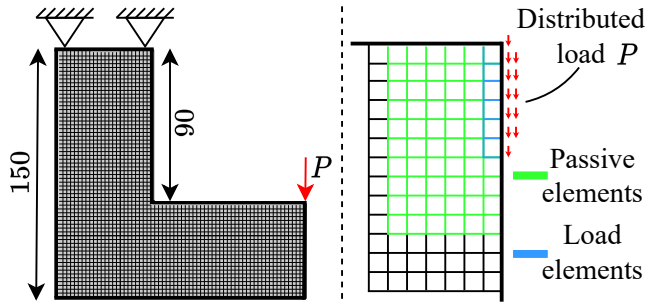

Fig. 2 L-bracket test case.

E_1	E_2	ν_{12}	G_{12}	X_t	X_c	Y_t	Y_c	S
137900	9000	0.3	7100	1950	1500	50	200	80

Tab. I Benchmark material data. The unit of all the strength and stiffness values is MPa.

The filter radius is 4 mm, and the threshold value in the projection filter κ is 0.5. β is initialized as 1 and doubled every tenth iteration until it reaches the maximum value. In order to avoid singularities in the load introduction the force $P = 1000\,\mathrm{N}$ is distributed on the 6 elements in a work equivalent manner, see Fig. 2. A grid of 6×10 elements around the load introduction is converted to passive elements. The densities have been initialized to the volume fraction 0.5, and the angles to the principal directions cf. [11]. The convergence criteria for the CFATO is based on the relative error of the objective function as defined in Eq. (42)

$$\frac{|c^{(k)} - c^{(k-1)}|}{c^{(k)}} \leq 10^{-5} \tag{42}$$

3.1 Optimization Without Stress Constraint

For the following numerical test, the stress constraint has not been included in the optimization. In Fig. 3 the resulting geometry is plotted. In Fig. 4 the corresponding Tsai-Wu failure indices have been plotted, with a focused view of the principal directions in the interface between structural members. Blue lines indicate compressive stress and red is a tensile stress. The length of the lines are normalized with respect to the largest principal stress in each element. The optimization converged in 108 iterations to a compliance of $1607\,\mathrm{mm/N}$. By removing the angle filter, it converges to a slightly lower compliance of $1592\,\mathrm{mm/N}$, however, at the cost of having a less smooth change in fiber orientation between elements in e.g. the sharp corner in Fig. 3. Filtering the angles imposes a more strict design space, due to the elements not being able to orient the fiber along the largest principal stress directions freely. As seen in Fig. 3, the resulting geometry has primarily smoothly varying fiber orientations. However, in the interfaces between tensile- and compressive stressed elements, the interfaces between structural members, two shortcomings are apparent: There are elements of intermediate densities and there is an abrupt change in

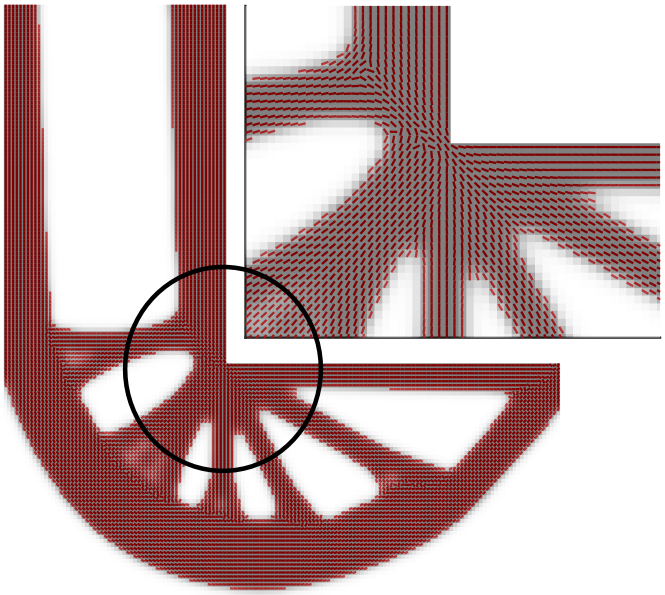

Fig. 3 Compliance-optimized L-bracket.

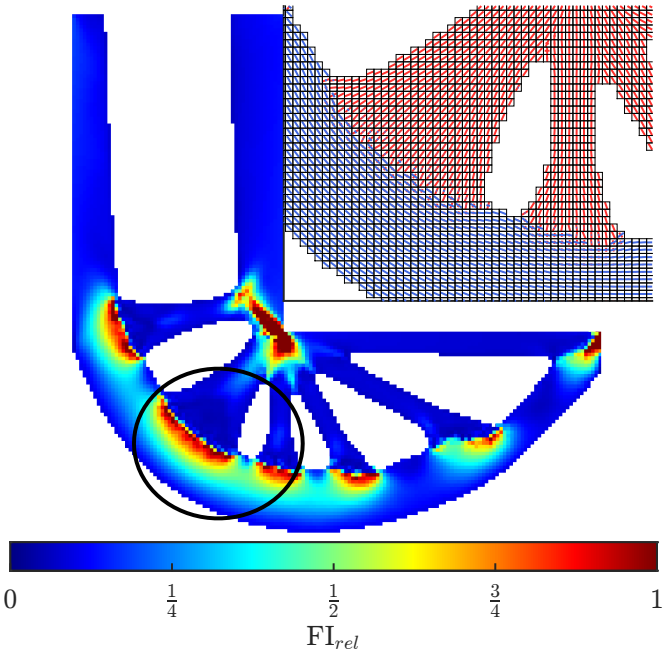

Fig. 4 Relaxed Tsai-Wu failure index of L-bracket and focused view of principal stress directions in the interface between structural members.

fiber orientation. This is also reflected in Fig. 4, where these elements have failure indices above 1. This is due to these elements experiencing compressive stresses and shearing, with the lowest material strength. The largest failure index of 5.5 is at the sharp corner, as seen on Fig. 4.

3.2 Optimization With Stress Constraint

For the following numerical tests, the stress constraint has been included in the optimization. In Fig. 5 the resulting geometry has been plotted and in Fig. 6 the corresponding Tsai-Wu failure indices have been plotted. The optimization converged in 1230 iterations to a compliance of $1855\,\mathrm{mm/N}$, with a maximum relaxed failure index is 0.991. Comparing Fig. 5 to Fig. 3, the sharp corner has been smoothed. It has not been removed entirely, as would be expected if trying to achieve the lowest stress state. Analogous to [13] and [15], stress-constrained optimization of the L-bracket showed alleviation, rather than removal, of the geometric stress concentration.

Additionally, the resulting compliance is higher than for the purely volume-constrained case, due to the stress constraint imposing a more strict feasible design space. The fiber angles are still primarily smooth, however, there are similar problems as in Section 3.1. Comparing Fig. 6 to Fig. 4, the introduction of the stress constraints results in additional, but narrower, structural members.

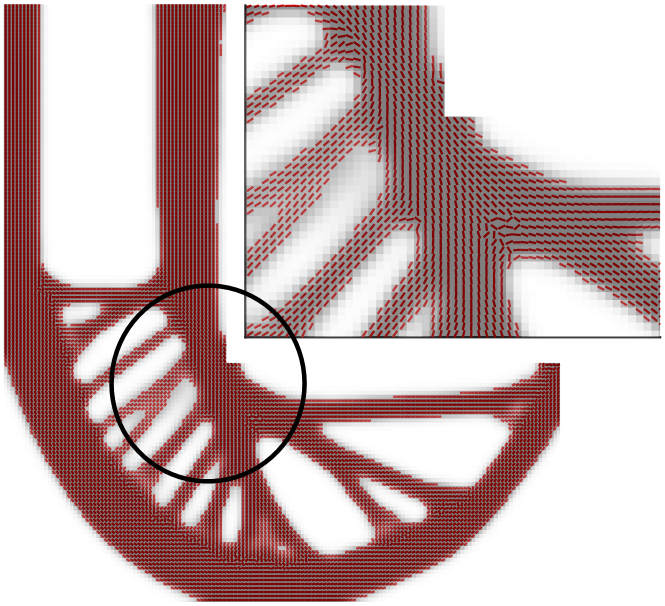

Fig. 5 Stress-constrained optimized L-bracket.

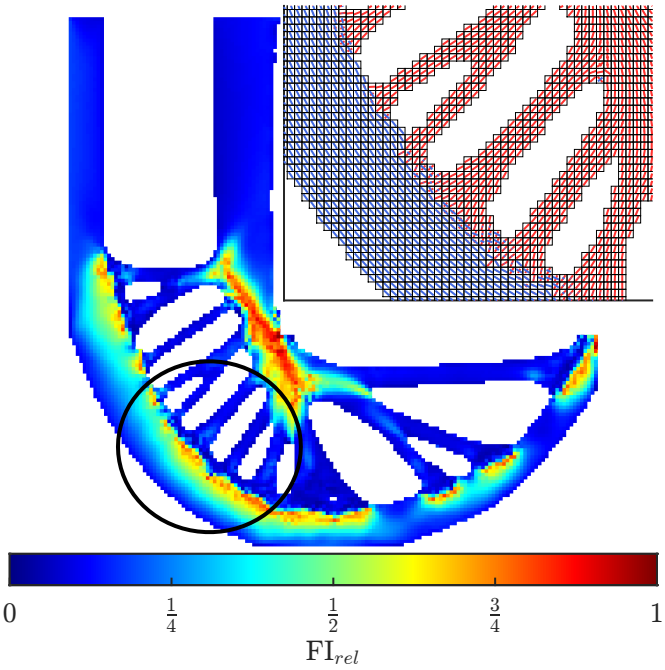

Fig. 6 Relaxed Tsai-Wu failure index of L-bracket and focused view of principal stress directions in the interface between structural members.

4. Post-processing and Manufacturing

4.1 Methodology

For this work, the streamline approach has been implemented for generating fiber paths, as it uses the fiber angles from the optimized design as input. Furthermore, with this method, manufacturing-tolerant paths can be generated. The Anisoprint Composer A4 used in this work has a minimum fiber length of 45 mm

and a line width of 0.75 mm. Minimum fiber length restrictions in the streamline algorithm is incorporated using the method presented by [22]. The path separation distance is set equal to the line width of the printer.

Although streamline methods are not ideal for creating continuous paths, the choice of seeding strategy may have an influence on the continuity of the paths. Basis for this work will therefore be to modify the MATLAB function 'Estream2' written by [27], to include four different seeding strategies for generating paths. This yields the following test cases;

1) No seed modifications: An established streamline creates new seed points orthogonal to the streamline at an offset of 0.75 mm.

2) Arbitrary seeding: All element center coordinates are supplied as potential seeds. New seeds continue in a column-major order according to Fig. 7.

3) Stress-based seeding: The starting point is the center coordinate of the element with the largest failure index. The next seed has the next-largest failure index etc.

4) Farthest-point seeding: The next seed is the unused coordinate where the smallest distance to all established streamlines is the largest.

For case 1), 2) and 4) the first seed is the center coordinate of the element in the upper-left of Fig. 7. For cases 2), 3) and 4), if a generated streamline has a length < 45 mm the seed is deleted, the streamline is not saved and no new seedpoints are generated. For all test cases, the stepsize is fixed at 0.5 mm and the streamline termination distance is equal to the separation distance of 0.75 mm.

Initial path-planning testing showed difficulties obtaining paths due to members in the optimization result being short compared to the minimum fiber length and also due to a coarse mesh. Therefore mesh refinement was introduced and the design domain increased to the maximum possible printable size on the Composer A4. Fig. 7 shows the test case used for generating toolpaths as well as the minimum fiber length.

Due to the periodicity of compliance, opposing vector orientations are apparent in the CFATO results. Therefore some vectors in Fig. 7 were flipped, to achieve the same vector orientation between most elements. This form of 'smoothing' does not change the optimization result as the element stiffness and stress remain the same when a fiber is rotated by 180°.

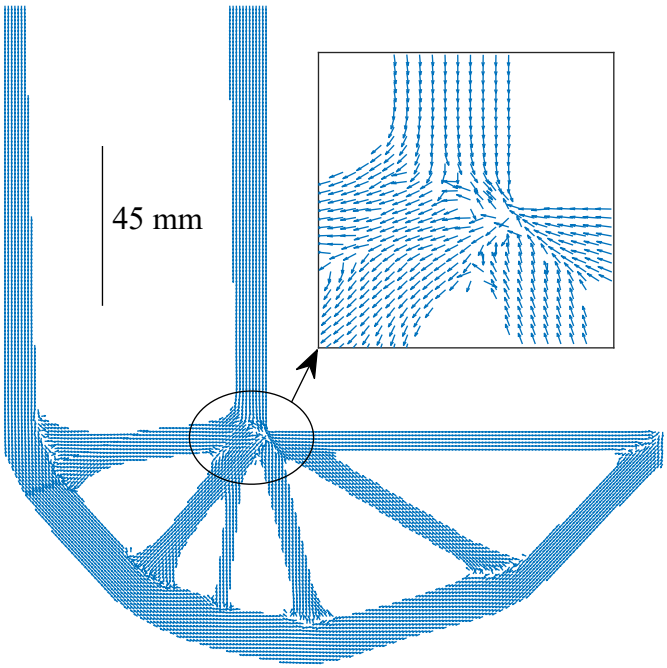

Fig. 7 Post-processing test case of stiffness-optimized design.

4.2 Post-processing Results and Discussion

Fig. 8 shows the print paths obtained using the stress-based seeding strategy.

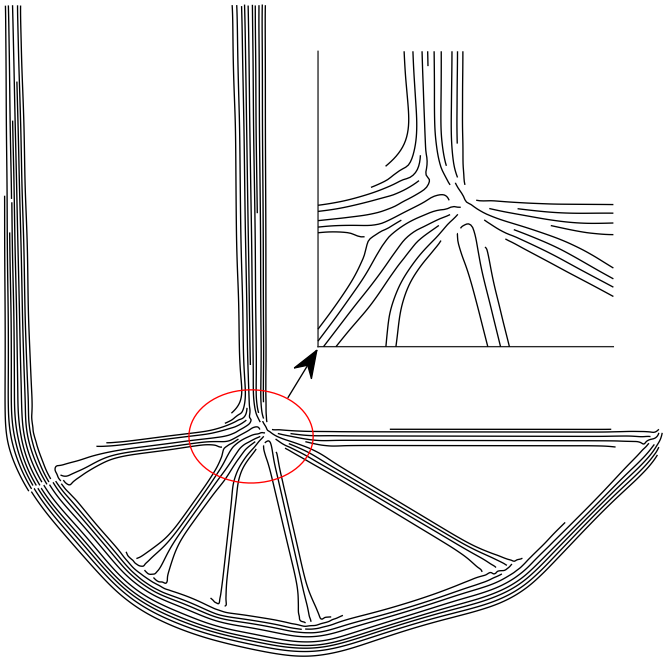

Fig. 8 Stress-based seeding (test case 3).

Arbitrary and farthest-point seeding (test case 2 and 4), generated similar results, hence only the stress-based seeding results are shown. Tab. II presents the number of generated paths, and average path length, for each seeding strategy.

Seeding	No. of paths	Avg. length
1. No modification	648	$\approx 11\,\mathrm{mm}$
2. Arbitrary	52	$\approx 107\,\mathrm{mm}$
3. Stress-based	52	$\approx 104\,\mathrm{mm}$
4. Farthest point	50	$\approx 108\,\mathrm{mm}$

Tab. II Test case results.

The results presented in Fig. 8 indicate good coverage of fiber paths over the field, which follow the optimized fiber orientations and are manufacturable by the CFC process. These results were obtained without prior smoothing of the field. For the presented field, arbitrary, stress-based and farthest-point seeding generates similar results. Although the latter generates slightly longer paths, it is not obvious which method is better based on this test case. Overall, results indicate gaps and a lack of continuity of fibers. The idea of stress-based seeding was to ensure fibers in highly-loaded locations, but due to a lack of continuity of the fibers, this is not ensured. To improve continuity, the input vector field may be altered to be bi-directional, such that paths are not stopped due to opposing vectors in the next step. Continuity may also be improved by connecting some paths after generation as done by [21] or formulating the path-planning in the optimization process.

4.3 Manufacturing

The Anisoprint slicer, Aura, is limited to certain continuous fiber infill methods and cannot print a single fiber along a given path. Thus, a custom G-code generator, capable of manufacturing the streamlines generated in Fig. 8, has been developed. It includes features used for the CFC 3D printing process, including cut-length distances before travel moves, and a travel algorithm that reduces the print time by selecting the shortest travel distance to a new print path. The G-code generator is limited to only following the paths determined by the streamlines, thus the streamline generation has a large effect on the mechanical properties of the manufactured part. In Fig. 9 a picture of the CFC 3D printed optimized design from Fig. 8 is seen. Some areas of the printed part do not coincide with each other and can not transfer loads. Thus, improvements should be performed to the path-planning, to ensure the structural integrity of the printed part.

5. Conclusion

A custom general-purpose FEA has been developed and utilized in CFATO under mass and Tsai-Wu failure index constraints. A streamline post-processing scheme has been implemented and the generated paths have been used in a G-code generator.

Fig. 9 The 3D printed CFRP specimen based on the topology optimized design in Fig. 7.

The mass-constrained optimization converged to a compliance of 1607 N/mm in 108 iterations. When including stress constraints, it rose to a compliance of 1855 N/mm in 1230 iterations.

The angle filter was able to produce primarily smooth fiber orientations, however, interfaces between compressive- and tensile-stressed members had significant changes in fiber orientations between elements. Due to these incoherent angles, the streamline generation caused gaps and a lack of continuity of the fibers. The results show that arbitrary, stress-based and farthest-point seeding generate similar results. However, due to the minimum fiber length being a part of the post-processing, rather than a constraint implemented in the optimization, the manufacturability of the optimized designs can not be guaranteed. It is suggested that further work should be done in order to improve continuity, either in the optimization or through post-processing. The custom G-code generator was able to accurately print the supplied streamlines.

While the current implementation may be preliminary, it demonstrates the potential for it to be a powerful design tool for CFC-manufactured structures.

Acknowledgement

The authors of this work gratefully acknowledge Grundfos for sponsoring the 11th MechMan symposium.

References

[1] N. Aage, E. Andreassen, B. S. Lazarov, and O. Sigmund, "Giga-voxel computational morphogenesis for structural design," Nature, vol. 550, pp. 84–86, 2017.

[2] M.-P. Schmidt, L. Coret, C. Gout, and C. B. Pedersen, "Structural topology optimization with smoothly varying fiber orientations," Struct Multidisc Optim, vol. 62, pp. 3105–3126, 2020.

[3] D. Jiang, R. Hoglund, and D. Smith, "Continuous fiber angle topology optimization for polymer composite deposition additive manufacturing applications," Fibers, vol. 7, no. 2, 2019.

[4] F. J. Gadegaard and J. Thuesen, "Strength based optimization and test of fiber reinforced additively manufactured structures considering topology and fiber orientation," 2022.

[5] O. Sigmund, "A 99 line topology optimization code written in matlab," Struct Multidisc Optim, vol. 21, pp. 120–127, 2001.

[6] A. Díaz and O. Sigmund, "Checkerboard patterns in layout optimization," Structural Optimization, vol. 10, no. 1, pp. 40–45, 1995.

[7] O. Sigmund, Design of material structures using topology optimization. PhD thesis, DTU, 1994.

[8] B. Bourdin, "Filters in topology optimization," Int. J. Num. Met. Eng., vol. 50, no. 9, pp. 2143–2158, 2001.

[9] T. Bruns and D. Tortorelli, "Topology optimization of non-linear elastic structures and compliant mechanisms," Comput Methods Appl Mech Eng, vol. 190, no. 26, pp. 3443–3459, 2001.

[10] J. Stegmann and E. Lund, "Discrete material optimization of general composite shell structures," Int. J. Num. Met. Eng., vol. 62, no. 14, pp. 2009–2027, 2005.

[11] P. Pedersen, "On optimal orientation of orthotropic materials," Structural Optimization, vol. 1, no. 2, pp. 101–106, 1989.

[12] C. Le, J. Norato, T. Bruns, C. Ha, and D. Tortorelli, "Stress-based topology optimization for continua," Struct Multidisc Optim, vol. 41, pp. 605–620, 2009.

[13] J. Oest and E. Lund, "Topology optimization with finite-life fatigue constraints," Struct Multidisc Optim, vol. 56, no. 5, pp. 1045–1059, 2017.

[14] E. Lund, "Discrete material and thickness optimization of laminated composite structures including failure criteria," Struct Multidisc Optim, vol. 57, no. 6, pp. 2357–2375, 2018.

[15] G. Ma, W. Yang, and L. Wang, "Strength-constrained simultaneous optimization of topology and fiber orientation of fiber-reinforced composite structures for additive manufacturing," Advances in structural engineering, vol. 25, no. 7, pp. 1636–1651, 2022.

[16] G. D. Cheng and X. Guo, "ε-relaxed approach in structural topology optimization," Struct Multidisc Optim, vol. 13, no. 4, pp. 258–266, 1997.

[17] M. Bruggi, "On an alternative approach to stress constraints relaxation in topology optimization," Struct Multidisc Optim, vol. 36, no. 2, pp. 125–141, 2008.

[18] A. Verbart, F. V. Keulen, and M. Langelaar, Topology Optimization with Stress Constraints. PhD thesis, TU Delft, 2015.

[19] G. A. da Silva, A. T. Beck, and O. Sigmund, "Stress-constrained topology optimization considering uniform manufacturing uncertainties," Comput Methods Appl Mech Eng, vol. 344, pp. 512–537, 2019.

[20] V. S. Papapetrou, C. Patel, and A. Y. Tamijani, "Stiffness-based optimization framework for the topology and fiber paths of continuous fiber composites," Composites part b, vol. 183, 2020.

[21] M. Eckrich, P. A. Arrabiyeh, A. M. Dlugaj, and D. May, "Structural topology optimization and path planning for composites manufactured by fiber placement technologies," Composite structures, vol. 289, 2022.

[22] J. R. Kubalak, A. L. Wicks, and C. B. Williams, "Deposition path planning for material extrusion using specified orientation fields," Procedia Manufacturing, vol. 34, pp. 754–763, 2019.

[23] M. Pedersen. ANSYSimport (https://www.mathworks.com/matlabcentral/fileexchange/66659-ansysimport, MATLAB Central File Exchange, 2023. Used 06-04-2023.

[24] R. D. Cook, D. S. Malkus, M. E. Plesha, and R. J. Witt, Concepts and applications of finite element analysis. N.Y: Wiley, 4 ed., 2001.

[25] R. M. Jones, Mechanics of Composite Materials. Taylor & Francis Inc., 2nd ed., 1998.

[26] K. Svanberg, "The method of moving asymptotes - a new method for structural optimization," Int. J. Num. Met. Eng., vol. 24, pp. 359–373, 1987.

[27] C. Thissen, estream2. https://github.com/cthissen/estream2, 2016. Used: 15-05-2023.